Highlights

- Technology adjustment and control effectively suppressed the cracks in the $V_{0.5}Nb_{0.5}ZrTi$ refractory high-entropy alloy during SLM process.
- Two different mechanisms of crack generation in the $V_{0.5}Nb_{0.5}ZrTi$ refractory high-entropy alloy were investigated.
- The microstructure and mechanical properties of the $V_{0.5}Nb_{0.5}ZrTi$ refractory high-entropy alloy were studied.

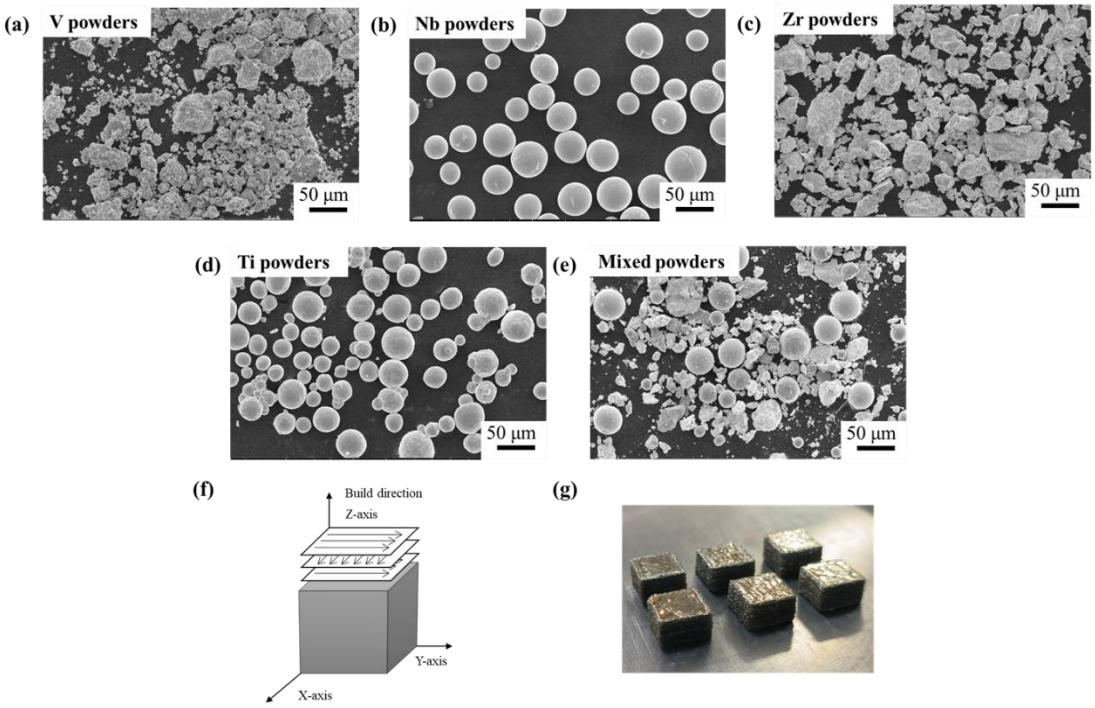

Fig. 1. SEM images of (a) V element powders, (b) Nb element powders, (c) Zr element powders and (d) Ti element powders; (e) mixed powders; (f) scanning strategy for SLM; (g) picture of the SLMed samples.

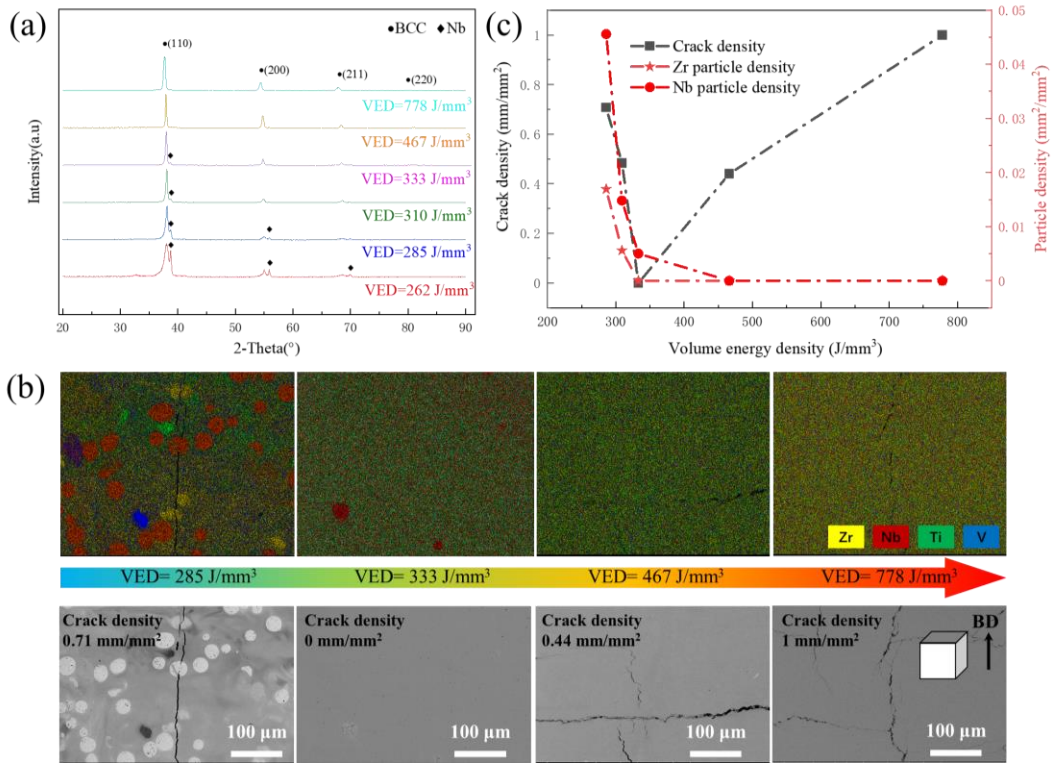

Fig. 2. (a) XRD patterns of the SLMed samples with different VEDs; (b) EDS elemental mapping images and BSD images of surface morphology of the SLMed samples with different VEDs; (c) dependences of average crack density and density of unmelted Zr (red star) and Nb (red circle) particles on VED.

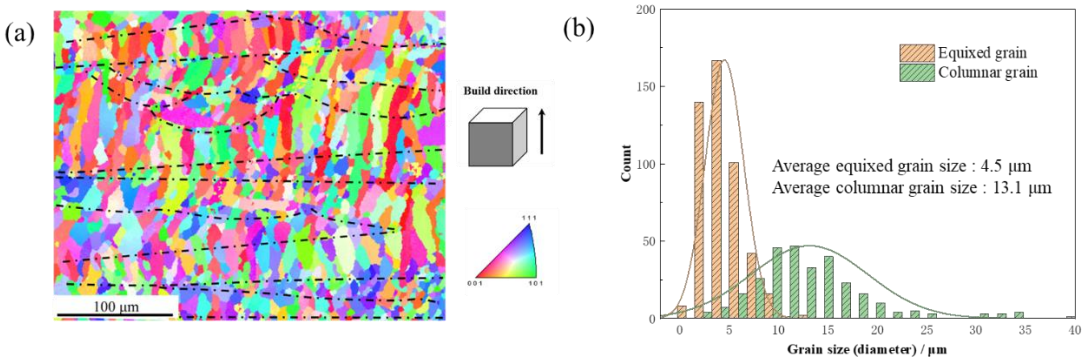

Fig. 3. (a) EBSD image of the SLMed sample with VED=333 J/mm^3, the bottoms of molten pool that are marked with black dotted lines; (b) grain size distributions of the SLMed sample with VED=333 J/mm^3.

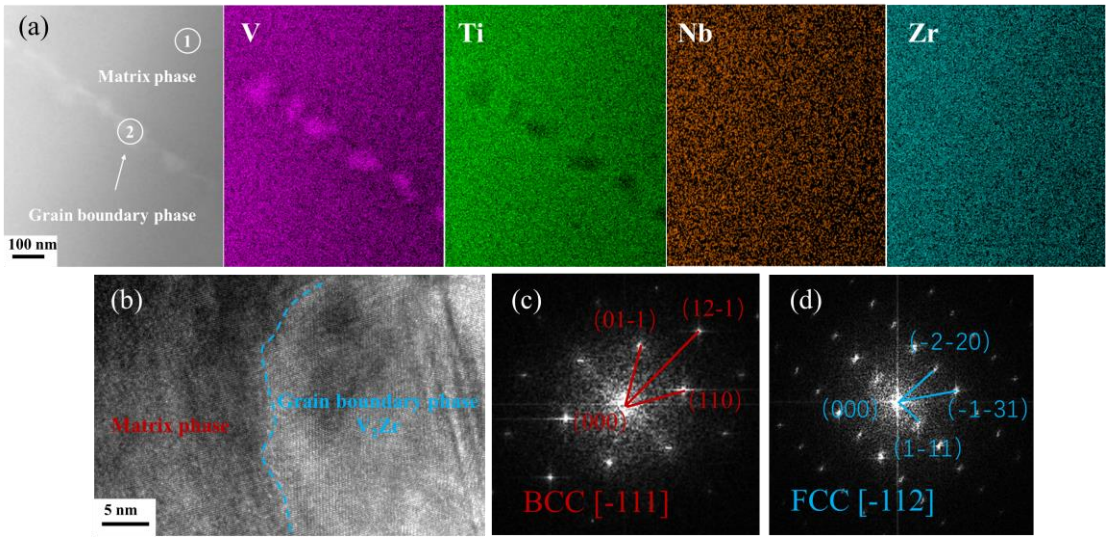

Fig. 4. (a) HAADF image and corresponding EDS elemental mapping images; (b) HRTEM image of the region around grain boundary; SAED patterns of the matrix phase (c) and grain boundary phase (d).

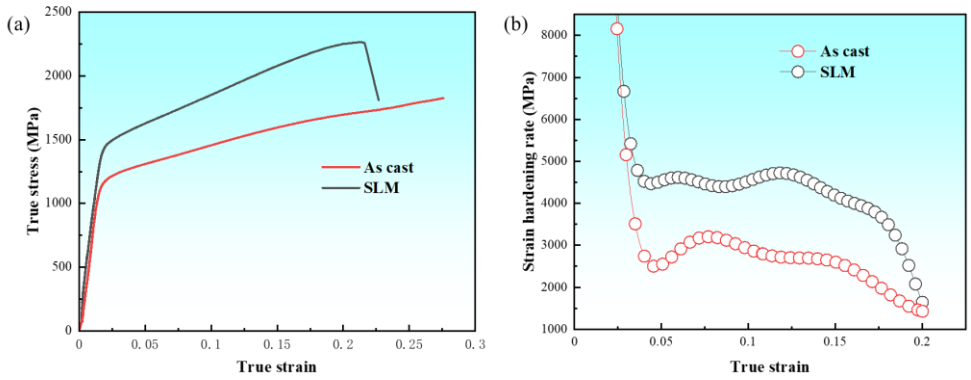

Fig. 5. (a) True stress-strain curves of the crack-free SLMed sample and the as-cast sample; (b) strain hardening rate curves of the crack-free SLMed sample and the as-cast sample.

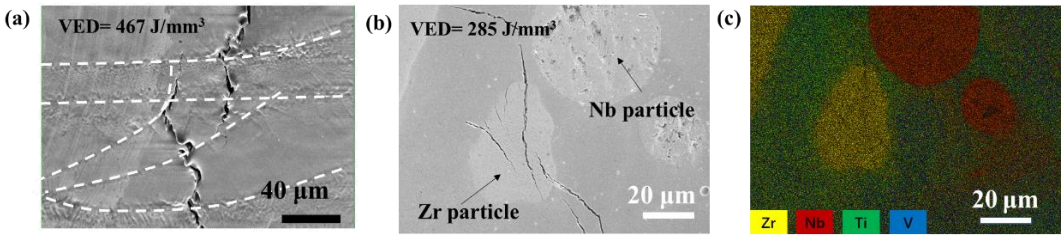

Fig. 6. (a) BSD image of the SLMed sample with VED=467 J/mm^3; (b) BSD image of the SLMed sample with VED=285 J/mm^3; (c) EDS elemental mapping image of the SLMed sample with VED=285 J/mm^3.

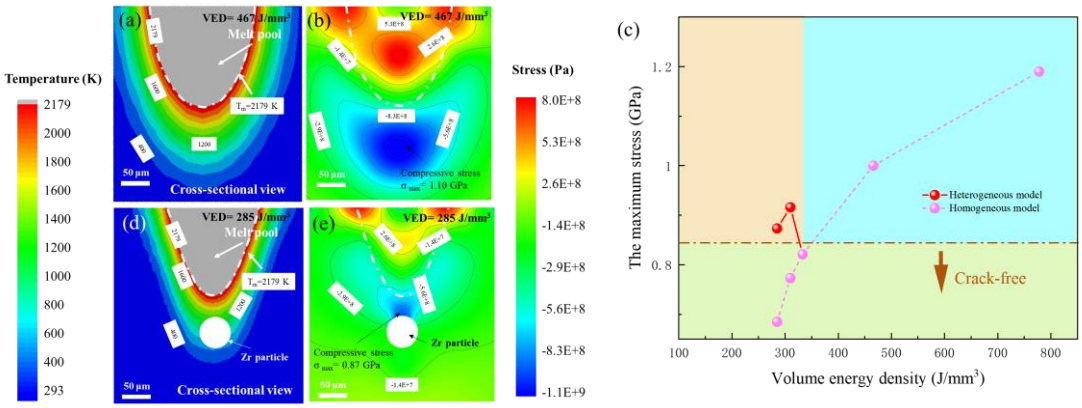

Fig. 7. Simulated temperature field (a) and thermal stress field (b) under homogeneous model with VED=467 J/mm^3; (c) dependence of the maximum stress on VED; simulated temperature field (d) and thermal stress field (e) under heterogeneous model with unmelted Zr particles and VED=285 J/mm^3.

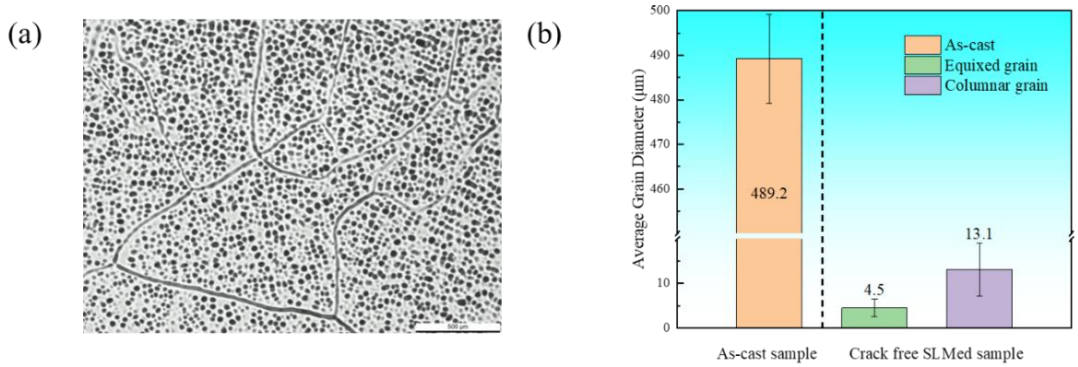

Fig. 8. (a) OM image of as-cast sample; (b) grain size distributions of the as-cast sample and the crack-free SLMed sample.

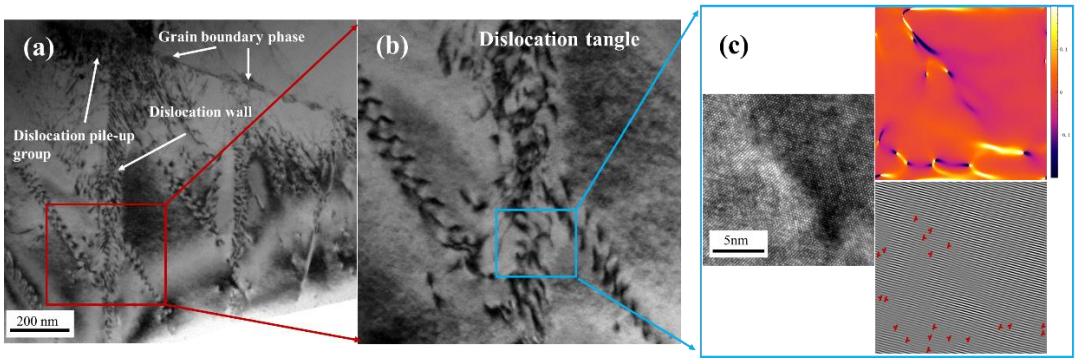

Fig. 9. (a) Bright-field TEM image of crack-free SLMed sample after a compression with 15% strain; (b) enlargement of the region in red rectangle; (c) HRTEM image, IFFT and a the corresponding e_{xx} distortion map in the region of blue rectangle.

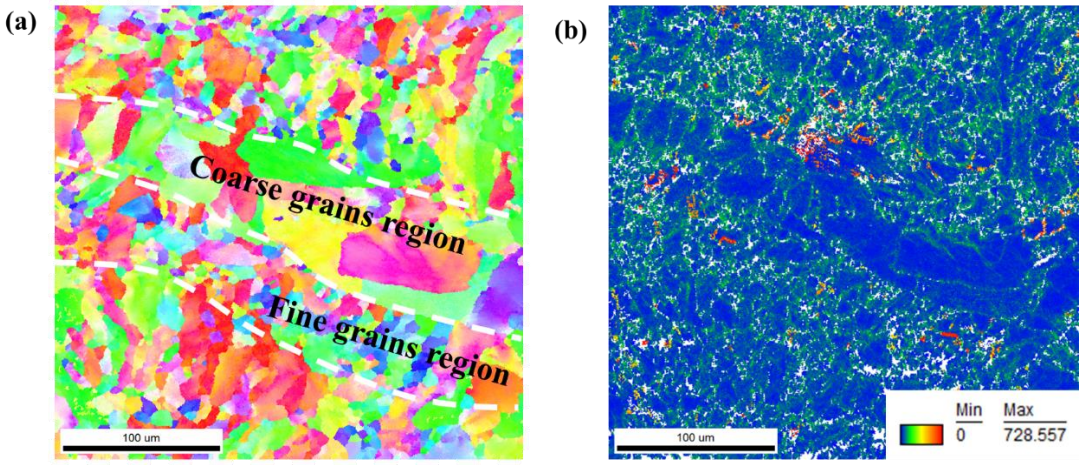

Fig. 10. (a) EBSD image of crack-free SLMed sample after the compression with 15% strain deformation; (b) the corresponding GND density distribution. The color bar in GNDs maps indicates the range of GND density from 1×10^{12} m^{-2} to 728×10^{12} m^{-2}.

$V_{0.5}Nb_{0.5}ZrTi$ refractory high-entropy alloy fabricated by laser addictive manufacturing using elemental powders

Peng Zhu[a], Yao Yu[a,*], Cheng Zhang[a], Qingjun Zhou[b], Bailing An[a], Rong Guo[a], K.C. Chan[c], Lin Liu[a,*]

a State Key Laboratory of Material Processing and Die & Mould Technology and School of Materials Science and Engineering, Huazhong University of Science and Technology, Wuhan 430074, China

b Capital Aerospace Machinery Corporation Limited, Beijing, 100076, China

c Department of Industrial and Systems Engineering, The Hong Kong Polytechnic University, Hung Hom, Kowloon, 999077, Hong Kong, China

* Corresponding authors

E-mail addresses: ensiyu@mail.hust.edu.cn (Y. Yu), lliu2000@mail.hust.edu.cn (L. Liu).

Highlights

- Technology adjustment and control effectively suppressed the cracks in the $V_{0.5}Nb_{0.5}ZrTi$ refractory high-entropy alloy during the SLM process.
- Two different mechanisms of crack generation in the $V_{0.5}Nb_{0.5}ZrTi$ refractory high-entropy alloy were investigated.
- The microstructure and mechanical properties of the $V_{0.5}Nb_{0.5}ZrTi$ refractory high-entropy alloy were studied.

Abstract

In this work, a $V_{0.5}Nb_{0.5}ZrTi$ refractory high-entropy alloy is successfully fabricated by the selective laser melting (SLM) method using elemental powders as precursors. A crack-free SLM-prepared (SLMed) sample with a nearly single BCC structure is acquired with a volume energy density (VED) of 333 J/mm^3. However, when the VED is lower or higher than 333 J/mm^3, microcracks are generated in the SLMed samples. The finite element method simulation reveals that there are two

mechanisms for generation of cracks. When VED < 333 J/mm^3, Zr particles are not completely melted. Cracks are formed around the Zr particles due to the crystalline structure and coefficient of thermal expansion mismatches between the unmelted Zr particles and the alloyed BCC matrix. When VED > 333 J/mm^3, cracks are formed due to thermal stress induced by the large temperature gradient during the SLM process. In addition, the SLMed crack-free sample exhibits much better mechanical properties than the as-cast counterpart. The current study provides a reference for the application of SLM technology to prepare refractory high-entropy alloys with excellent mechanical properties using elemental powders as the precursor.

Key words: Refractory high-entropy alloy; Selective laser melting; Finite element method simulation; Mechanical property.

1. Introduction

Refractory high-entropy alloys (RHEAs) are highly promising new alloy systems consisting of various refractory elements (Cr, Hf, Mo, Nb, Ta, V, W, Zr, Ti) mixed in equal or nearly equimolar ratios[1-3]. Compared with conventional nickel-based high-temperature alloys, RHEAs have excellent mechanical properties as well as unique properties such as resistance to high-temperature oxidation[4-6] and corrosion[7,8] at both room and high temperatures due to the decreased diffusion rate and increased lattice distortion[9-11]. Therefore, RHEAs are expected to be used at higher temperatures and become the next generation of high-temperature alloys that show a wide range of application prospects[4]. The commonly used methods to fabricate RHEAs include

vacuum arc melting, mechanical alloying and spark plasma sintering processes[12-15]. For instance, the CrHfNbTaTi RHEA[12] was prepared by a vacuum-arc melting process. This RHEA is composed of one FCC phase and two BCC phases, and exhibits excellent mechanical properties. The $Al_{0.1}$CrNbVMo RHEA[13] was prepared by the mechanical alloying and spark plasma sintering processes. The density of the alloy is lower than those of most nickel-based superalloys. The compressive strength of the alloy is 2863 MPa at room temperature and exceeds 1400 MPa at 1000 °C. However, due to the high melting point and poor machinability, the conventional manufacturing of RHEA parts normally incurs high costs and restrained shapes[2], limiting their range of applicability.

Recently, additive manufacturing (AM) technology has attracted wide attention due to its advantages of high precision, high efficiency, and the ability to easily manufacture complex-shaped parts[16-18]. AM technology has been introduced to fabricate near-net-shape RHEA parts, and many studies have focused on AM of RHEAs in terms of processing investigations, microstructures and mechanical properties[19-27]. Among the AM techniques, selective laser melting (SLM) has a high cooling rate (10^4–10^6 K/s) during the manufacturing processes, which favors the formation of refined microstructures[28,29] and enhances the mechanical properties of the printed products[30-35]. The SLM process was first employed to manufacture WTaMoNb[23] and then many other RHEAs, including TiNbTaZrMo[24], NbMoTaTi$_{0.5}$Ni$_{0.5}$[25] and WMoTaTi[26]. The SLM-prepared (SLMed) RHEAs exhibit excellent performance in some respects. For instance, the SLMed WTaMoNb RHEA[23] exhibits high hardness as well as excellent corrosion resistance compared with the as-cast counterpart. However, there are still

some problems that need to be solved in the preparation of RHEAs by the SLM method.

Generally, elemental powders are used as the precursor in the SLM process. Because of the high melting point of each element of the RHEA, achieving uniform alloying is the primary problem. Certainly, this problem can be circumvented by using pre-alloyed RHEA powders as raw materials. For instance, pre-alloyed $Ti_{1.4}Nb_{0.6}Ta_{0.6}Zr_{1.4}Mo_{0.6}$ RHEA powders were used as precursors to prepare RHEAs with low porosity, customizable shape, excellent yield stress, and good biocompatibility[24]. In addition, pre-alloyed powders prepared by mechanical alloying and gas-solid fluidization were used for SLM formation of WMoTaTi RHEA[26], resulting in a SLMed WMoTaTi with a relative density of 95.8% and a microstructure consisting of BCC solid solution and HCP-Ti precipitates. However, the preparation of pre-alloyed RHEA powders is complicated, costly and impractical due to the extremely high melting point of the elements. The most obvious way to solve the uniform alloying problem is to increase the input power in the SLM process. However, with increasing laser energy input, there will be another serious problem, i.e., cracking due to the generation of a steep temperature gradient around melt pools. The high temperature gradient would induce huge thermal stress and lead to the occurrence of cracking in the SLMed samples[36,37]. Several attempts have been made to solve the cracking problem. For instance, introducing low melting temperature FCC grain boundary phases can generate a large number of layer dislocations to release the thermal stress in the SLM process. One example is that the cracking problem was suppressed in the preparation of $MoNbTaTi_{0.5}Ni_{0.5}$ RHEA[25]. However, the introduction of a large amount of low

melting temperature grain boundary phase significantly reduced the high temperature mechanical properties of RHEA. Therefore, achieving better alloying and suppressing cracking at the same time without introducing a large amount of intermetallic compounds is an urgent problem to be solved for the preparation of RHEA by the SLM process.

In this work, we report that a $V_{0.5}Nb_{0.5}ZrTi$ RHEA was successfully fabricated by the SLM method using elemental powders as the precursor. By carefully manipulating the printing parameters, we succeeded in printing a sample with a high degree of alloying and without occurrence of cracking. Further combined with finite element method (FEM) simulation, we elucidated the correlation between alloying and cracking. Finally, the mechanical properties of the SLMed sample were tested and compared with those of the as-cast sample. The results show that the SLMed sample exhibits much better mechanical properties than the as-cast sample.

2. Experimental procedures

2.1. Materials and process

Pure V, Nb, Zr and Ti powders (purity > 99%) were used as raw materials. Fig. 1 shows scanning electron microscopy (SEM) images of the powders. The average diameter of all the powders is approximately 15–45 μm. Ti and Nb powders are spherical, while V and Zr powders are irregular in shape. The V, Nb, Zr and Ti elemental powders were evenly mixed by mechanical ball milling in a vacuum jar with a molar ratio of 1:1:2:2. The theoretical atomic percentage of each element and the estimated melting point of $V_{0.5}Nb_{0.5}ZrTi$ RHEA are shown in Table 1.

Self-developed SLM equipment was used for 3D printing of the $V_{0.5}Nb_{0.5}ZrTi$ RHEA. The SLM equipment was equipped with a fiber laser with a beam spot of 80 μm, wavelength of 1060 nm and maximum output power of 500 W. To investigate the effect of defects on mechanical properties, a set of experiments with various volume energy densities ($VED = P/vht$[38], where P is the laser power, v is the scanning speed, h is the hatch spacing and t is the powder layer thickness) were conducted with the cross-hatching strategy. Here, h and t were fixed at h= 60 μm and t = 40 μm, respectively, while v and P were varied from 300 to 700 mm/s and from 220 to 280 W, respectively. The scan directions were parallel to the X- and Y-directions, and the Z-axis was the building direction of the sample, as shown in Fig. 1e. There was an additional remelting process, which had the same parameters as the original process. Titanium alloy was used as the substrate. The as-fabricated samples were cuboid with dimensions of approximately 5× 5 × 5 mm^3 (Fig. 1f).

For comparison, the as-cast samples with the same composition were prepared by a vacuum arc melting process using pure metals of V, Nb, Zr and Ti (>99.95 wt %). The ingots were re-melted at least 5 times inside a water-cooled copper cavity to improve the chemical homogeneity.

2.2.Characterization

The microstructure was characterized by using optical microscope (OM, Leica DFC 450) and scanning electron microscopy (SEM, Quanta650 FEG), equipped with an energy dispersive X-ray spectrometer (EDS) and electron backscattered diffraction (EBSD) analyzer. Phase analysis was carried out by using an X-ray diffractometer

(XRD, 7000SX, Shimadzu). The detailed structure of the SLMed samples was also characterized using transmission electron microscopy (TEM, 07 Tecnai G2 F30) and selected area electron diffraction (SAED). The compression tests were performed using a Zwick machine (Roell 020) at a strain rate of 10^{-4} s^{-1}. The strain rate was controlled by the displacement rate of the crosshead, referring to the elastic part. The compression specimens had dimensions of φ2 mm × 4 mm. For the quantification of cracking of each sample, the polished three longitudinal cross-sections were analyzed by OM. Image-Pro Plus software was employed to measure the total cracking length. Then the average cracking density was defined as the total cracking length over the measured area[39]. Here, we used the average cracking density to evaluate the cracking susceptibility of samples fabricated with different processing parameters.

2.3. FEM simulation

For the FEM simulation, a sequentially 3D coupled thermo-mechanical model was performed by commercial ABAQUS software, from which the temperature fields and thermal stress fields during various SLM processes were calculated. The constitutive equations and calculation procedures are illustrated in detail in the Supplementary Materials. The specific heat capacity, thermal conductivity, and thermal diffusivity were measured by a laser thermal conductivity instrument (LFA-427). The thermal-physical properties of the $V_{0.5}Nb_{0.5}ZrTi$ RHEA and process parameters (such as laser power, scanning speed, etc.) used in the simulations are listed in Table 2 and Table 3, respectively.

3. Results

3.1. Microstructure of the SLMed $V_{0.5}Nb_{0.5}ZrTi$ RHEA

The alloying status of the elements and the structure of the SLMed samples with different VEDs were primarily examined by XRD experiments, as shown in Fig. 2a. When the VED is 262 J/mm^3 (the lowest value in this study), the XRD pattern shows two sets of diffraction peaks. One set corresponds to a phase with the BCC structure, which is the alloyed phase as the matrix. The other set refers to the unmelted Nb particles due to their high melting point. As the VED increases, the Nb peaks become weaker. When the VED is 467 J/mm^3, the Nb peaks completely disappear, suggesting that the degree of alloying also increases with increasing VED.

The SLMed samples were further characterized by SEM observations. Fig. 2b shows the EDS elemental mapping images and the corresponding SEM images of three typical samples processed with VED=285 J/mm^3, 333 J/mm^3, 467 J/mm^3 and 778 J/mm^3. The EDS elemental mapping images display the alloying degree of the samples. Many unmelted Nb particles together with a small amount of other elements (most of which are Zr particles) can be clearly discerned with the VED of 285 J/mm^3. However, the Zr particles are fully melted, and only a small amount of Nb particles remain when the VED increases to 333 J/mm^3. With the VED further increasing, the unmelted Nb particles become fewer and completely disappear with VED=467 J/mm^3, suggesting that the sample is fully alloyed at this energy state. The detailed dependences of the density of the unmelted particles (Nb (circle) and Zr (star)) on VED are plotted in Fig. 2c.

In addition, the SEM images reflect the cracking of the samples, which is also closely related to the VED value. The average crack density of the sample with various VEDs is shown in Fig. 2c. It decreases sharply with increasing VED from 285 J/mm^3 to 333 J/mm^3 but gradually increases when the VED increases from 333 J/mm^3 to 778 J/mm^3. It should be noted that a crack-free sample is only obtained with VED=333 J/mm^3. The above phenomenon indicates that there should be two different mechanisms for the generation of microcracks in the SLMed RHEA, which will be discussed in the next section.

The microstructure of the crack-free sample obtained with VED=333 J/mm^3 is further examined. The grain size distribution of the sample was characterized by EBSD, as shown in Fig. 3. The SLMed sample consists of a heterogeneous lamellar structure with alternating coarse and fine grain zones. The columnar coarse grains exist inside the melt pool, while the equiaxed fine grains are located at the bottom of melt pool. The average grain size of coarse grains is approximately 13.1 μm and that of fine grains is approximately 4.5 μm. Here, the solidification progress cannot be well comprehended based on conventional solidification theory[40], which mainly takes the balance between the temperature gradient and growth into consideration. Under the action of a high-energy laser beam, the previously solidified part is re-melted, and the dendrite tip can be detached and then transported into the melt, acting as a favorable nucleation site[24]. The formation of fine grains could result from the increased nucleation frequency at the bottom of the melt pool. The bottoms of the melt pools that exist between layers called as layer-layer melt pool boundaries[41] are marked with black dotted lines in Fig. 3a. In

the YZ-plane, the melt pool transverse cross-section formed by the X-scan with the semi-elliptical shape and the longitudinal melt pool cross-section formed by the Y-scan running horizontally were stacked alternately along the Z-direction. During further solidification steps, the existing grains in the fine grain zone grow into the liquid in the direction opposite to heat dissipation, leading to the formation of coarse columnar grains in melt pools[42,43].

Fig. 4 shows the TEM images of the crack-free sample (prepared with VED=333 J/mm^3). The high-angle annular dark field (HAADF) image (Fig. 4a) reveals that there are some precipitates at the grain boundary (GB) with a size of approximately 200 nm. The precipitates are enriched in V and depleted in Ti as indicated by EDS elemental mapping images (Fig. 4a), while the composition is homogenous inside the grains, indicating that the SLMed sample is well alloyed although the elemental powders were used as the precursor. The detailed elemental analyses of the matrix phase (Position 1) and the GB phase (Position 2) are summarized in Table 4. The composition of the matrix (i.e., inside the grains) is close to the nominal composition of $V_{0.5}Nb_{0.5}ZrTi$, while the composition of the GB phase is close to V_2Zr. Fig. 4b shows the high-resolution TEM (HRTEM) image around the GB. The SAED suggests that the matrix is of the BCC structure (Fig. 4c), which is consistent with the XRD result. However, the nanophase at the grain boundaries is of the FCC structure of V_2Zr (Fig. 4d). It is normally the case that low melting point intermetallic compounds precipitate preferentially at the GBs when the molten alloy starts to solidify[44] during the SLM process. In fact, the phase diagrams show that among the four elements, only V and Zr form a low-melting point

intermetallic compound (V_2Zr)[45]. The lattice constant of the grain boundary phase calculated from the TEM results is 7.72 Å, which is slightly larger than the standard lattice constant of 7.44 Å for V_2Zr. The slight expansion of the lattice can be understood as the solid solution of Nb. As a result, the grain boundary phase should be V_2Zr with a small portion of V substituted by Nb.

3.2.Mechanical properties of SLMed $V_{0.5}Nb_{0.5}ZrTi$ RHEA

The mechanical properties of the crack-free SLMed sample were examined by compression. Fig. 5a shows the true stress-true strain curves of the sample. Note that the curve of the as-cast sample is also included for comparison. Compared with the as-cast sample, the SLMed sample displays much better compression properties. The yield strength increases to 1450 MPa, which is nearly 1.4 times that of the as-cast sample (1050 MPa). In addition, the SLMed sample exhibits a higher strain hardening rate than the as-cast sample, as shown in Fig. 5b.

4. Discussion

4.1. Microcracks in the SLMed RHEAs

As the results show above, the average crack density decreases with VED below 333 J/mm^3, but increases with VED above 333 J/mm^3, which indicates that there are different mechanisms of the generation of microcracks in SLMed RHEAs with VED below and above the critical value of 333 J/mm^3. To explore the mechanisms for cracking, the microstructure of two typical samples with VED=467 J/mm^3 (higher than 333 J/mm^3) and VED=285 J/mm^3 (lower than 333 J/mm^3) were carefully examined.

Fig. 6a shows the SEM image of the sample with VED=467 J/mm^3, where the white dotted lines mark the position of the melt pool boundaries. In this high VED condition, the sample was fully alloyed, and a large number of microcracks were found at the melt pool boundaries. Fig. 6b shows the SEM image of the sample with VED=285 J/mm^3, and the corresponding EDS elemental mapping image is shown in Fig. 6c. In this low VED condition, there are many unmelted particles, and the initial positions of the microcracks are quite different. The microcracks are mainly found in the interior of the Zr particles and at the edge of their contact with the matrix. These results suggest that the generation of microcracks is related to the preparation process when the VED is above 333 J/mm^3, but is related to the unmelted Zr particles when the VED is below 333 J/mm^3.

To further explore the two mechanisms of generation of microcracks, FEM simulations were performed to explore the thermal stress during the SLM process, which is believed to be the main cause of cracking[46]. First, a homogeneous model is considered, in which the sample is alloyed uniformly without unmelted particles. Fig. 7a and 7b show the simulated temperature field and thermal stress field with VED=467 J/mm^3. There is a steep temperature gradient created at the edge of the melt pool (marked by the white dashed line). The generation of this temperature gradient is caused by the rapid heating of the upper surface by the focused laser beam[36]. As a result, there is a concentration of stress at the edge of the melt pool (marked by the white dashed line) with the maximum stress located near the bottom of the melt pool. Moreover, the temperature gradient increases with increasing VED. This leads to an increase in the

maximum stress. The simulated maximum stress values at different VEDs are plotted in Fig. 7c (purple circle).

Second, a heterogeneous model with unmelted Zr particles is considered. Fig. 7d and 7e show the simulated temperature field and thermal stress field with VED=285 J/mm^3. Certainly, there is a stress concentration at the edge of the melt pool due to the steep temperature gradient. However, there is an additional stress concentration (0.87 GPa) around the unmelted Zr particles, which is closely related to temperature. The generation of this additional stress concentration is mainly related to differences in the crystalline structure and the coefficient of thermal expansion between the Zr particles and the RHEA matrix. On the one hand, the crystalline structure of Zr is HCP, which is different from the BCC structure of the matrix. On the other hand, the coefficient of thermal expansion of Zr (5.7×10^{-6} K^{-1}) is much smaller than that of the RHEA matrix (7.4×10^{-6} K^{-1}), and both factors contribute to the generation of stress concentrations around the Zr particles. As the crystalline structure and coefficient of thermal expansion mismatches between the unmelted Zr particles and the alloyed BCC matrix are mainly related to the temperature around the Zr particles which increases slightly with VED, the maximum stress value around the Zr particles also increases slightly with VED, as shown in Fig. 7c (red circle). Note that no cracks were observed around the unmelted Nb particles. To understand the cause, the temperature field and thermal stress field are also simulated with VED=285 J/mm^3, as shown in Fig. S3. The maximum stress value (0.73 GPa) is just slightly higher than that simulated from the homogeneous model (0.69 GPa). Because the crystalline structure of Nb is the same as the RHEA matrix

(both are of BCC structure), and the coefficient of thermal expansion of Nb (7.3×10^{-6} K^{-1}) and the RHEA matrix (7.4×10^{-6} K^{-1}) are quite similar, the additional concentration of stress due to the mismatch of the unmelted Nb particles and the RHEA matrix is negligible.

The above analysis reveals the two mechanisms of the thermal stress concentration under different process conditions. When VED > 333 J/mm^3, there are no unmelted Zr particles, and the thermal stress maximum is determined by the temperature gradient created in the SLM process. The temperature gradient increases with increasing VED, resulting in an increase in crack density. When VED < 333 J/mm^3, the thermal stress maximum is mainly caused by the mismatches between the unmelted Zr particles and the RHEA matrix. The maximum value of thermal stress does not vary significantly with VED. Under this condition, the crack density is determined by the density of Zr particles. As a result, the unmelted Zr particles decrease with increasing VED, leading to a decrease in crack density.

As shown in Fig. 7c, the maximum stress shows a minimum value with VED=333 J/mm^3; therefore, a crack-free sample was obtained at this critical VED value. In addition, it is worth noting that the maximum thermal stress that the sample can withstand without cracking coincides with the ultimate tensile strength of the as-cast sample. This seems to provide a crack-free criterion for SLMed RHEA samples. However, more work should be done to validate this criterion.

4.2. Strengthening of the crack-free SLMed $V_{0.5}Nb_{0.5}ZrTi$ RHEA

For the crack-free SLMed sample, the mechanical tests show that the SLMed sample has a much higher yield strength (1450 MPa) than that of the as-cast counterpart (1050 MPa). Here, the yield strength, σ_y, of $V_{0.5}Nb_{0.5}ZrTi$ RHEA can be expressed as:

$$\sigma_y = \sigma_0 + \Delta\sigma_{GB} + \Delta\sigma_p \quad (1)$$

where σ_0, $\Delta\sigma_{GB}$ and $\Delta\sigma_p$ are the lattice friction resistance, the strength contributed by GB strengthening, and the strength contributed by precipitation strengthening, respectively. The GB strengthening effect due to this grain refinement can be calculated by the Hall-Patch[47] equation:

$$\Delta\sigma_{GB} = k_y d^{-1/2} \quad (2)$$

where, k_y is the GB strengthening coefficient (k_y = 1366 MPa $\mu m^{1/2}$[48]), and *d* is the average grain size.

Fig. 8a shows the OM image of the as-cast sample. The average grain size of the as-cast sample is 489.2 μm, and the GB strengthening contribution of the cast sample is 62 MPa. The grain size of the SLMed sample is substantially smaller, as shown in Fig. 8b. Taking the heterogeneous grained structure and their volume fractions into account, i.e., *d* (grain size) = 4.5 μm and φ (volume fraction) = 16% in the equiaxed fine grain zone and *d* = 13.1 μm and φ = 84% in the columnar coarse grain zone, the $\Delta\sigma_{GB}$ values from the equiaxed fine grain zone and columnar coarse grain zone are calculated as 103 MPa and 307 MPa, respectively, giving a total contribution of 410 MPa from GB strengthening. Therefore, the increment of the yield strength brought by grain refinement is 348 MPa, which is slightly smaller than the yield strength

difference between the SLMed sample and the cast sample (400 MPa), indicating that the yield strength increase mainly results from grain refinement. In addition, the V_2Zr precipitates at grain boundaries could also play some role in strengthening the SLMed sample.

Fig. 9a shows the TEM image of the crack-free SLMed sample after compression with 15% strain. A large number of dislocations are plugged at the grain boundaries and the regions around the GB phase. Such stacking of the dislocations around the precipitates at the GB suggests that the GB phase hinders dislocation movements, and contributes to the strengthening of the sample. Moreover, the dislocations inside the grains are heavily entangled with each other, and form dislocation walls during the deformation process. The enlarged picture of the dislocation entanglement region (Fig. 9b) and the corresponding HRTEM, strain distribution and dislocation configuration (Fig. 9c) show that a large number of dislocations and strains are present in this region. These entangled dislocations impede the subsequent motion of other dislocations. Thus, the presence of these grain boundaries, second phases, and dislocation entanglements would contribute to the increase in the yield strength and would further greatly improve the strain-hardening rate of the SLMed sample during deformation.

Moreover, the heterogeneous structure with alternating arrangements of fine and coarse grains may also contribute to the good strain-hardening capacity in the post-yielding [49,50]. Fig. 10 shows the EBSD image and the corresponding geometrically necessary dislocations (GNDs) image of the SLMed sample compressed with 15%

strain. Similar to the sample before deformation, the sample after deformation also shows a structure with obvious heterogeneous grains. However, compared with the GND density distribution of the sample before deformation (see Fig. S4), the GND density of the deformed sample is greatly increased. In addition, the GND density shows a heterogeneous distribution. The high GND density points are mainly distributed in the fine grain region, while the low GND density points are mainly distributed in the coarse grain region, indicating that the nonuniform distribution of GND density is caused by the heterogeneous structure. The nonuniform distribution of GNDs can generate hetero-deformation induced (HDI) stress[51]. The HDI stress may inhibit the dislocation source inside the columnar grain region from emitting dislocations. Thus, additional stresses are required to make the dislocation source to further emit dislocations[52-55]. Therefore, the presence of a heterogeneous structure creates HDI stress and enhances the strain-hardening rate of the SLMed sample.

5. Conclusions

A novel $V_{0.5}Nb_{0.5}ZrTi$ RHEA was fabricated via the SLM process using elemental powders produced by mechanical mixing with ball milling. The mechanism of crack generation of the SLMed $V_{0.5}Nb_{0.5}ZrTi$ RHEA has been studied in detail. Consequently, high forming capability and strength for SLM can only be obtained with a small process window. The main conclusions can be summarized as follows:

1. The $V_{0.5}Nb_{0.5}ZrTi$ RHEA shows severe cracking during the SLM process. When VED < 333 J/mm^3, Zr particles are not completely melted. The thermal stress

maximum is caused by the crystalline structure and coefficient of thermal expansion mismatches between the unmelted Zr particles and the substrate. When VED > 333 J/mm^3, the thermal stress maximum is determined by the temperature gradient. The maximum stress shows a minimum value with VED=333 J/mm^3, and a crack-free sample was obtained at this critical VED value.

2. The microstructure and mechanical properties of the SLMed $V_{0.5}Nb_{0.5}ZrTi$ RHEA were investigated. The SLMed samples exhibit a heterogeneous lamellar grain pattern with alternating coarse and fine grains and significant grain refinement compared to the as-cast samples. The yield strength of the crack-free SLMed sample is approximately 1450 MPa, which is nearly 1.4 times that of the as-cast sample (1050 MPa). In addition, the SLMed sample exhibits a much higher strain hardening rate than the as-cast sample.

CRediT authorship contribution statement

Peng Zhu: Investigation, Methodology, Experiments, Writing – original draft. Yao Yu: Formal analysis, Visualization, Writing & editing. Cheng Zhang: Formal analysis. Bailing An: Formal analysis. Rong Guo: Formal analysis. K.C. Chan: Writing & editing, Funding acquisition. Lin Liu: Resources, Supervision, Writing & editing, Funding acquisition.

Declaration of Competing Interest

The authors declare that they have no known competing financial interests or personal relationships that could have appeared to influence the work reported in this paper.

Acknowledgements

The work described in this paper was substantially supported by the National Natural Science Foundation of China (NSFC)/Research Grants Council of Hong Kong (RGC) Joint Research Scheme (Grant No. 52061160483 and No. N_PolyU523/20). The authors are also grateful to the Analytical and Testing Center, Huazhong University of Science and Technology for technical assistance.

References

[1] Senkov O N, Wilks G B, Miracle D B. Refractory high-entropy alloys[J]. Intermetallics, 2010, 18(9): 1758-1765.

[2] Srikanth M, Annamalai A R, Muthuchamy A, Jen C-P. A Review of the Latest Developments in the Field of Refractory High-Entropy Alloys[J]. Crystals, 2021, 11(6): 612.

[3] Senkov O N, Miracle D B, Rao S I. Correlations to improve room temperature ductility of refractory complex concentrated alloys[J]. Materials Science and Engineering A, 2021(19): 141512.

[4] Senkov O N, Miracle D B, Chaput K J, Couzinie J-P. Development and exploration of refractory high entropy alloys—A review[J]. Journal of Materials Research, 2018, 33(19): 3092-3128.

[5] Gorr B, Mueller F, Christ H J, Mueller T, Chen H, Kauffmann A, et al. High temperature oxidation behavior of an equimolar refractory metal-based alloy 20Nb20Mo20Cr20Ti20Al with and without Si addition[J]. Journal of Alloys and Compounds, 2016, 688: 468-477.

[6] Ouyang D, Chen Z-J, Yu H-B, Chan K C, Liu L. Oxidation behavior of the Ti38V15Nb23Hf24 refractory high-entropy alloy at elevated temperatures[J]. Corrosion Science, 2022, 198: 110153.

[7] Yan D, Song K, Sun H, Wu S, Zhao K, Zhang H, et al. Microstructures, Mechanical Properties, and Corrosion Behaviors of Refractory High-Entropy ReTaWNbMo Alloys[J]. Journal of Materials Engineering and Performance,

2020, 29(1): 399-409.
[8] Hung S-B, Wang C-J, Chen Y-Y, Lee J-W, Li C-L. Thermal and corrosion properties of V-Nb-Mo-Ta-W and V-Nb-Mo-Ta-W-Cr-B high entropy alloy coatings[J]. Surface and Coatings Technology, 2019, 375: 802-809.
[9] George E P, Curtin W A, Tasan C C. High entropy alloys: A focused review of mechanical properties and deformation mechanisms[J]. Acta Materialia, 2020, 188: 435-474.
[10] Gorsse S, Miracle D B, Senkov O N. Mapping the world of complex concentrated alloys[J]. Acta Materialia, 2017, 135: 177-187.
[11] Bhandari U, Zhang C, Guo S, Yang S. First-principles study on the mechanical and thermodynamic properties of MoNbTaTiW[J]. International Journal of Minerals, Metallurgy and Materials, 2020, 27(10): 1398-1404.
[12] Yi J, Tang S, Zhang C, Xu M, Yang L, Wang L, et al. Microstructure and Mechanical Properties of a New Refractory Equiatomic CrHfNbTaTi High-Entropy Alloy[J]. JOM, 2021, 73(3): 934-940.
[13] Kang B, Lee J, Ryu H J, Hong S H. Microstructure, mechanical property and Hall-Petch relationship of a light-weight refractory Al0.1CrNbVMo high entropy alloy fabricated by powder metallurgical process[J]. Journal of Alloys and Compounds, 2018, 767: 1012-1021.
[14] Senkov O N, Wilks G B, Scott J M, Miracle D B. Mechanical properties of Nb25Mo25Ta25W25 and V20Nb20Mo20Ta20W20 refractory high entropy alloys[J]. Intermetallics, 2011, 19(5): 698-706.
[15] Pan J, Dai T, Lu T, Ni X, Dai J, Li M. Microstructure and mechanical properties of Nb25Mo25Ta25W25 and Ti8Nb23Mo23Ta23W23 high entropy alloys prepared by mechanical alloying and spark plasma sintering[J]. Materials Science and Engineering: A, 2018, 738: 362-366.
[16] Zhang C, Zhu J, Zheng H, Li H, Liu S, Cheng G J. A review on microstructures and properties of high entropy alloys manufactured by selective laser melting[J]. International Journal of Extreme Manufacturing, 2020, 2(3): 032003.
[17] Arif Z U, Khalid M Y, Ur Rehman E, Ullah S, Atif M, Tariq A. A review on laser cladding of high-entropy alloys, their recent trends and potential applications[J]. Journal of Manufacturing Processes, 2021, 68: 225-273.
[18] Zhang T, Liu C-T. Design of titanium alloys by additive manufacturing: A critical review[J]. Advanced Powder Materials, 2022, 1(1): 100014.
[19] Zhang H, Zhao Y, Huang S, Zhu S, Wang F, Li D. Manufacturing and Analysis of High-Performance Refractory High-Entropy Alloy via Selective Laser Melting (SLM)[J]. Materials (Basel), 2019, 12(5).
[20] Dobbelstein H, Thiele M, Gurevich E L, George E P, Ostendorf A. Direct Metal Deposition of Refractory High Entropy Alloy MoNbTaW[J]. Physics Procedia, 2016, 83: 624-633.
[21] Melia M A, Whetten S R, Puckett R, Jones M, Heiden M J, Argibay N, et al. High-throughput additive manufacturing and characterization of refractory high entropy alloys[J]. Applied Materials Today, 2020, 19: 100560.
[22] Kunce I, Polanski M, Bystrzycki J. Microstructure and hydrogen storage

properties of a TiZrNbMoV high entropy alloy synthesized using Laser Engineered Net Shaping (LENS)[J]. International Journal of Hydrogen Energy, 2014, 39(18): 9904-9910.

[23] Zhang H, Xu W, Xu Y, Lu Z, Li D. The thermal-mechanical behavior of WTaMoNb high-entropy alloy via selective laser melting (SLM): experiment and simulation[J]. The International Journal of Advanced Manufacturing Technology, 2018, 96(1): 461-474.

[24] Ishimoto T, Ozasa R, Nakano K, Weinmann M, Schnitter C, Stenzel M, et al. Development of TiNbTaZrMo bio-high entropy alloy (BioHEA) super-solid solution by selective laser melting, and its improved mechanical property and biocompatibility[J]. Scripta Materialia, 2021, 194: 113658.

[25] Zhang H, Zhao Y, Cai J, Ji S, Geng J, Sun X, et al. High-strength NbMoTaX refractory high-entropy alloy with low stacking fault energy eutectic phase via laser additive manufacturing[J]. Materials & Design, 2021, 201: 109462.

[26] Liu C, Zhu K, Ding W, Liu Y, Chen G, Qu X. Additive manufacturing of WMoTaTi refractory high-entropy alloy by employing fluidised powders[J]. Powder Metallurgy, 2022, 65(5): 413-425.

[27] Moorehead M, Bertsch K, Niezgoda M, Parkin C, Elbakhshwan M, Sridharan K, et al. High-throughput synthesis of Mo-Nb-Ta-W high-entropy alloys via additive manufacturing[J]. Materials & Design, 2020, 187: 108358.

[28] Li Q, Zhang H, Li D, Chen Z, Wang F, Wu M. Comparative study of the microstructures and mechanical properties of laser metal deposited and vacuum arc melted refractory NbMoTa medium-entropy alloy[J]. International Journal of Refractory Metals and Hard Materials, 2020, 88: 105195.

[29] Kong D, Dong C, Wei S, Ni X, Zhang L, Li R, et al. About metastable cellular structure in additively manufactured austenitic stainless steels[J]. Additive Manufacturing, 2021, 38: 101804.

[30] Suryawanshi J, Prashanth K G, Scudino S, Eckert J, Prakash O, Ramamurty U. Simultaneous enhancements of strength and toughness in an Al-12Si alloy synthesized using selective laser melting[J]. Acta Materialia, 2016, 115: 285-294.

[31] Wang Y M, Voisin T, Mckeown J T, Ye J, Calta N P, Li Z, et al. Additively manufactured hierarchical stainless steels with high strength and ductility[J]. Nat Mater, 2018, 17(1): 63-71.

[32] Liu L, Ding Q, Zhong Y, Zou J, Wu J, Chiu Y-L, et al. Dislocation network in additive manufactured steel breaks strength–ductility trade-off[J]. Materials Today, 2018, 21(4): 354-361.

[33] Zhu Z G, Nguyen Q B, Ng F L, An X H, Liao X Z, Liaw P K, et al. Hierarchical microstructure and strengthening mechanisms of a CoCrFeNiMn high entropy alloy additively manufactured by selective laser melting[J]. Scripta Materialia, 2018, 154: 20-24.

[34] Prashanth K G, Scudino S, Klauss H J, Surreddi K B, Löber L, Wang Z, et al. Microstructure and mechanical properties of Al–12Si produced by selective laser melting: Effect of heat treatment[J]. Materials Science and Engineering: A, 2014, 590: 153-160.

[35] Zhou P F, Xiao D H, Wu Z, Ou X Q. Al0.5FeCoCrNi high entropy alloy prepared by selective laser melting with gas-atomized pre-alloy powders[J]. Materials Science and Engineering: A, 2019, 739: 86-89.
[36] Liu F, Lin X, Yang G, Song M, Chen J, Huang W. Microstructure and residual stress of laser rapid formed Inconel 718 nickel-base superalloy[J]. Optics & Laser Technology, 2011, 43(1): 208-213.
[37] Zhang S, Lin X, Chen J, Huang W. Influence of Heat Treatment on Residual Stress of Ti-6Al-4V Alloy by Laser Solid Forming[J]. Xiyou Jinshu Cailiao Yu Gongcheng/Rare Metal Materials and Engineering, 2009, 38: 774-778.
[38] Simchi A, Pohl H. Effects of laser sintering processing parameters on the microstructure and densification of iron powder[J]. Materials Science and Engineering: A, 2003, 359(1): 119-128.
[39] Guo B, Zhang Y, Yang Z, Cui D, He F, Li J, et al. Cracking mechanism of Hastelloy X superalloy during directed energy deposition additive manufacturing[J]. Additive Manufacturing, 2022, 55: 102792.
[40] Yan F, Xiong W, Faierson E. Grain Structure Control of Additively Manufactured Metallic Materials[J]. Materials, 2017, 10: 1260.
[41] Karthik G M, Kim H S. Heterogeneous Aspects of Additive Manufactured Metallic Parts: A Review[J]. Metals and Materials International, 2021, 27(1): 1-39.
[42] Bermingham M J, Stjohn D H, Krynen J, Tedman-Jones S, Dargusch M S. Promoting the columnar to equiaxed transition and grain refinement of titanium alloys during additive manufacturing[J]. Acta Materialia, 2019, 168: 261-274.
[43] Rai A, Helmer H, Körner C. Simulation of grain structure evolution during powder bed based additive manufacturing[J]. Additive Manufacturing, 2017, 13: 124-134.
[44] Cloots M, Uggowitzer P J, Wegener K. Investigations on the microstructure and crack formation of IN738LC samples processed by selective laser melting using Gaussian and doughnut profiles[J]. Materials & Design, 2016, 89: 770-784.
[45] Cui J, Guo C, Zou L, Li C, Du Z. Thermodynamic modeling of the V–Zr system supported by key experiments[J]. Calphad, 2016, 53: 122-129.
[46] Mercelis P, Kruth J-P. Residual stresses in selective laser sintering and selective laser melting[J]. Rapid Prototyping Journal, 2006, 12.
[47] Hansen N. Hall–Petch relation and boundary strengthening[J]. Scripta Materialia, 2004, 51(8): 801-806.
[48] Li X T. Study of the microstructure and mechanical properties of Ti-Zr-Nb-V-Al high-entropy alloy (in chinese)[D]. Shenyang: Northeastern University, 2020. https://doi.org/ 10.27007/d.cnki.gdbeu.2020.001003.
[49] Wu X, Yang M, Yuan F, Wu G, Wei Y, Huang X, et al. Heterogeneous lamella structure unites ultrafine-grain strength with coarse-grain ductility[J]. Proc Natl Acad Sci U S A, 2015, 112(47): 14501-5.
[50] Wu X, Yang M, Li R, Jiang P, Yuan F, Wang Y, et al. Plastic accommodation during tensile deformation of gradient structure[J]. Science China Materials, 2021, 64(6): 1534-1544.

[51] Zhu Y, Wu X. Perspective on hetero-deformation induced (HDI) hardening and back stress[J]. Materials Research Letters, 2019, 7: 393 - 398.
[52] Feaugas X. On the origin of the tensile flow stress in the stainless steel AISI 316L at 300 K: back stress and effective stress[J]. Acta Materialia, 1999, 47(13): 3617-3632.
[53] Mughrabi H. Dislocation wall and cell structures and long-range internal stresses in deformed metal crystals[J]. Acta Metallurgica, 1983, 31(9): 1367-1379.
[54] Gibeling J G, Nix W D. A numerical study of long range internal stresses associated with subgrain boundaries[J]. Acta Metallurgica, 1980, 28(12): 1743-1752.
[55] Wu X, Jiang P, Chen L, Yuan F, Zhu Y T. Extraordinary strain hardening by gradient structure[J]. Proc Natl Acad Sci U S A, 2014, 111(20): 7197-201.

Table 1
The theoretical composition and melting point of $V_{0.5}Nb_{0.5}ZrTi$ RHEA.

alloy element (at.%)	V	Nb	Zr	Ti	Melting point (K)
$V_{0.5}Nb_{0.5}ZrTi$	16.67	16.67	33.33	33.33	2179

Table 2
Thermo-physical properties of $V_{0.5}Nb_{0.5}ZrTi$ RHEA.

Temperature, (K)	Thermal diffusivity, a ($\times 10^{-6} m^2 s^{-1}$)	Specific heat capacity, c ($\times 10^3$ $Jkg^{-1}K^{-1}$)	Thermal conductivity, K_{bulk} ($Wm^{-1}K^{-1}$)
295.9	3.478	0.37	7.87
473.3	4.857	0.36	10.7
673.3	6.307	0.25	9.53
874.2	6.993	0.24	10.31
1074.2	7.927	0.32	15.41
1273.9	8.557	0.37	19.24
1473.6	8.468	0.39	20.17

Table 3
Parameters for finite element simulation of SLM $V_{0.5}Nb_{0.5}ZrTi$ RHEA.

Parameters	Value
Laser power, P (W)	200-300
Scanning speed, v (m s^{-1})	0.3-0.7
Laser beam spot size, d (m)	8×10^{-5}
Effective laser beam radius, $a=\frac{d/2}{2.146}$ (m)	2.33×10^{-5}
Laser absorption length, λ (m)	1.06×10^{-6}
Laser absorptivity, $A = 0.365\sqrt{\omega/\lambda}$, in which ω = 128μΩ is the resistivity	0.404
Density of RHEA ρ (kg m^{-3})	6500
Melting point, T_m (K)	2179
Thermal expansion coefficient, α (K^{-1})	7.4×10^{-6}
Young's modulus, E (GPa)	103.83
Poisson's ratio, ν	0.30
Stefan-Boltzmann constant, σ ($Wm^{-2}K^{-4}$)	5.67×10^{-8}
Radiation emissivity, ε	0.77
Heat transfer coefficient, h_c ($Wm^{-2}K^{-1}$)	20

Table 4
The elemental distribution in the matrix phase and GB phase of $V_{0.5}Nb_{0.5}ZrTi$ alloy.

alloy element (at.%)	V	Nb	Zr	Ti
Position-1	18.69	20.41	27.34	33.56
Position-2	52.11	16.57	22.66	8.65

Supplementary Materials for $V_{0.5}Nb_{0.5}ZrTi$ refractory high-entropy alloy fabricated by laser addictive manufacturing using elemental powders

Peng Zhu[a], Yao Yu[a,*], Cheng Zhang[a], Qingjun Zhou[b], Bailing An[a], Rong Guo[a], K.C. Chan[c], Lin Liu[a,*]

a State Key Laboratory of Material Processing and Die & Mould Technology and School of Materials Science and Engineering, Huazhong University of Science and Technology, Wuhan 430074, China

b Capital Aerospace Machinery Corporation Limited, Beijing, 100076, China

c Department of Industrial and Systems Engineering, The Hong Kong Polytechnic University, Hung Hom, Kowloon, 999077, Hong Kong, China

* Corresponding authors

E-mail addresses: ensiyu@mail.hust.edu.cn (Y. Yu), lliu2000@mail.hust.edu.cn (L. Liu).

Due to the complexity of the SLM process, we have made some simplifications to make the simulation available[1]: (1) the whole powder bed is regarded as an isotropic continuum, and SLM process is stable. Consequently, the characteristics of molten pool, such as fluxion, molten pool size, are assumed to be constant; (2) the mass flow in molten pools during phase transition is ignored; (3) the introduced un-melted particles are ideally spherical.

A thermal-mechanical coupled analysis model was established by ABAQUS software, as shown in Fig. S1. A Gaussian distributed moving heat flux was applied via an ABAQUS subroutine DFLUX. The dimension of the computational model is 2.5×2.5×0.5 mm^3. In order to optimize the computation time and accuracy during SLM process, elements were finely meshed with brick element of 30 μm. Therefore, 49972 elements were involved totally, and C3D8T elements were selected for analysis[2]. The detailed algorithms for the temperature distribution and thermal stress distribution are presented as follows.

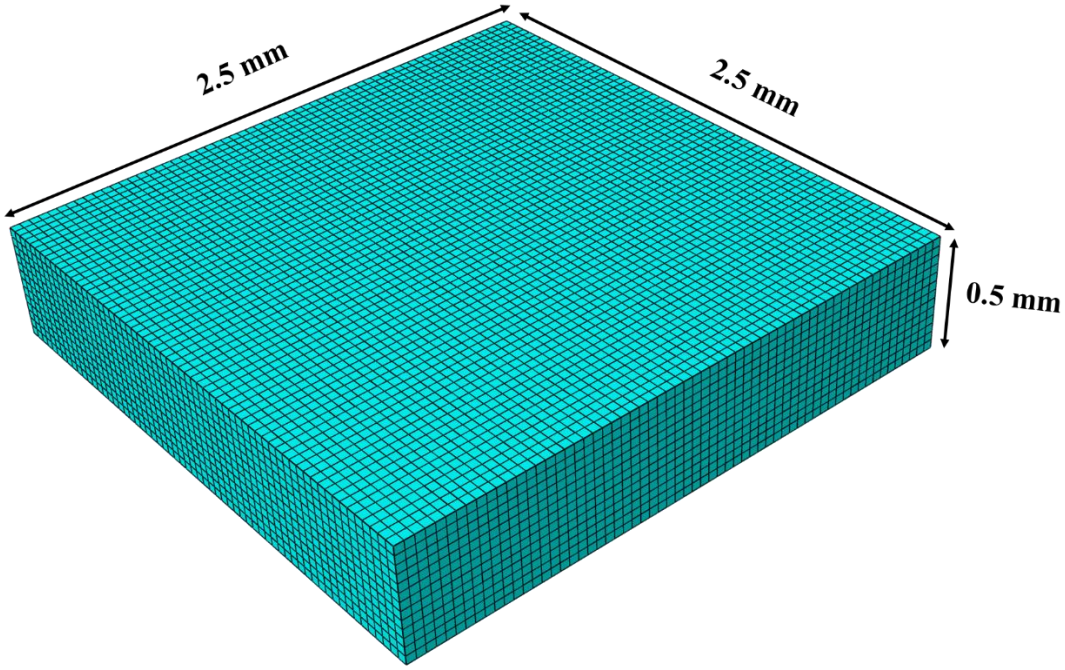

Fig.S1 Three-dimensional coupled thermo-mechanical finite element model

Thermal analysis

In simulation work, the energy density, $q(x,y,z)$, absorbed by the powder bed from laser beam is assumed to obey a Gaussian distribution, and was modeled using DFLUX subroutine, which can be expressed by the following equation[3]:

$$q(x,y,z) = \frac{9AQ}{\pi H R_0^2 \left(1-\frac{1}{e^3}\right)} exp\left[\frac{-9}{R_0^2\, log\left(\frac{H}{z}\right)}(x^2+y^2)\right] \quad (1)$$

in which x, y and z are the coordinates; H, R_0 are the height and mouth diameter of the heat source; Q is the laser power; A is the energy absorptivity of the $V_{0.5}Nb_{0.5}ZrTi$ RHEA.

The boundary conditions for heat transfer can be described as:

$$q(x,y,z) = q_{cond} + q_c + q_r \quad (2)$$

where q_{cond}, q_c, q_r are the heat losses through conduction, convection and radiation in the model, respectively, and can be defined as follows[4]:

$$q_{cond} = -k\Delta T \quad (3)$$

$$q_c = h_c(T - T_0) \quad (4)$$

$$q_r = \sigma\varepsilon(T^4 - T_0^4) \quad (5)$$

where k is the thermal conductivity coefficient, ΔT is the temperature gradient

between different materials, $h_c$is heat transfer coefficient, σ is the Stefan-Boltzman constant, ε is the radiation emissivity, T is the temperature of melting pool, T_0 is the ambient temperature. The thermal initial condition at $t = 0$ can be defined as[1]:

$$T(x, y, z, t)|t_0 = 0, x, y, z \in D = T_0 = 296K \tag{6}$$

It is assumed that the transient spatial distribution of the temperature field $T(x, y, z, t)$ satisfies the following equation[5]:

$$\rho \frac{\partial \left(c_p(T)T\right)}{\partial t} = \frac{\partial}{\partial x}\left(k(T)\frac{\partial T(x,y,z,t)}{\partial x}\right) + \frac{\partial}{\partial y}\left(k(T)\frac{\partial T(x,y,z,t)}{\partial y}\right) + \frac{\partial}{\partial z}\left(k(T)\frac{\partial T(x,y,z,t)}{\partial z}\right) \tag{7}$$

where ρ is the density of the $V_{0.5}Nb_{0.5}ZrTi$ RHEA, $c_p(T)$ and $k(T)$, depending on the temperature, are the specific heat capacity, thermal conductivity of the $V_{0.5}Nb_{0.5}ZrTi$ RHEA, respectively; $T(x, y, z, t)$ is the temperature at point (x, y, z) at time t; x, y and z are the coordinates. In addition, the latent heat of fusion during the phase transformation should be considered, and the relationship can be described as[6] :

$$H = \int \rho c_p dT \tag{8}$$

Stress analysis

As along as the temperature field is determined, the thermal load is subsequently applied for thermal stress analysis. By implementing the small deformation theory the total strain can be calculated as[7]:

$$d\varepsilon = d\varepsilon_e + d\varepsilon_p + d\varepsilon_t \tag{9}$$

where $d\varepsilon$, $d\varepsilon_e$, $d\varepsilon_p$ and $d\varepsilon_t$ are the increment of total strain, elastic strain, plastic strain and thermal strain, respectively. The components of stress and strain are defined as[8]:

$$d\sigma = \left[d\sigma_{xx}\ d\sigma_{yy}\ d\sigma_{zz}\ d\sigma_{xy}\ d\sigma_{yz}\ d\sigma_{xz}\right]^T$$
$$d\varepsilon = \left[d\varepsilon_{xx}\ d\varepsilon_{yy}\ d\varepsilon_{zz}\ d\varepsilon_{xy}\ d\varepsilon_{yz}\ d\varepsilon_{xz}\right]^T \tag{10}$$

where the increment of total strain $d\varepsilon$ is determined by the displacement increment $du = [du\ dv\ dw]^T$, and the relation is given as:

$$d\varepsilon = Bdu \tag{11}$$

where B is the matrix relating the displacement and strain; du is derived by

$$du = \frac{F^{app} - F^{nr}}{K} \tag{12}$$

in which F^{app}, F^{nr} are the externally applied force and Newton–Raphson restoring force obtained from the element internal loading, K is the stiffness matrix.

The increment of elastic strain $d\varepsilon_{el}$, plastic strain $d\varepsilon_{pl}$ and thermal strain $d\varepsilon_{t}$ are given as[9]:

$$d\varepsilon_e = Dd\sigma \tag{13}$$

$$d\varepsilon_p = d\lambda\left\{\frac{\partial f}{\partial \sigma}\right\} \tag{14}$$

$$d\varepsilon_t = A\Delta T \tag{15}$$

in which D is elasticity matrix, A is the coefficient matrix of thermal expansion, $d\lambda$ is the hardening parameter, f is derived by the yield function[10]:

$$f = \sigma_{von} - \sigma_{yield} \tag{16}$$

in which σ_{yield} is the yield stress, σ_{von} is the von Mises stress, and defined as[11]

$$\sigma_{von} = \sqrt{\frac{3}{2}(S-\alpha)^T(S-\alpha)} \tag{17}$$

where S is the deviatoric stress tensor, α is the yield surface translation tensor, and determined by

$$\alpha = \int C d\varepsilon_{pl} \tag{18}$$

in which C is the material parameter.

The substrate is fixed in the SLM process, which is defined by the boundary conditions as follows:

$$\begin{aligned} x = \pm X &: u = 0 \\ y = \pm Y &: v = 0 \\ z = -Z &: \omega = 0 \end{aligned} \tag{19}$$

in which u, v and ω are the displacements in the x, y and z directions, respectively.

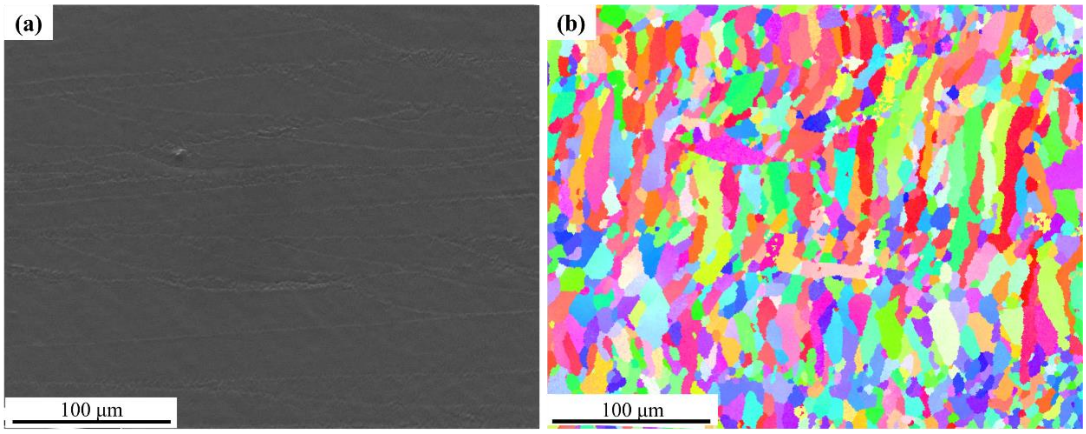

Fig. S2 (a) SEM image after electrolytic polishing and (b) corresponding EBSD image of the SLMed sample with VED=333 J/mm^3

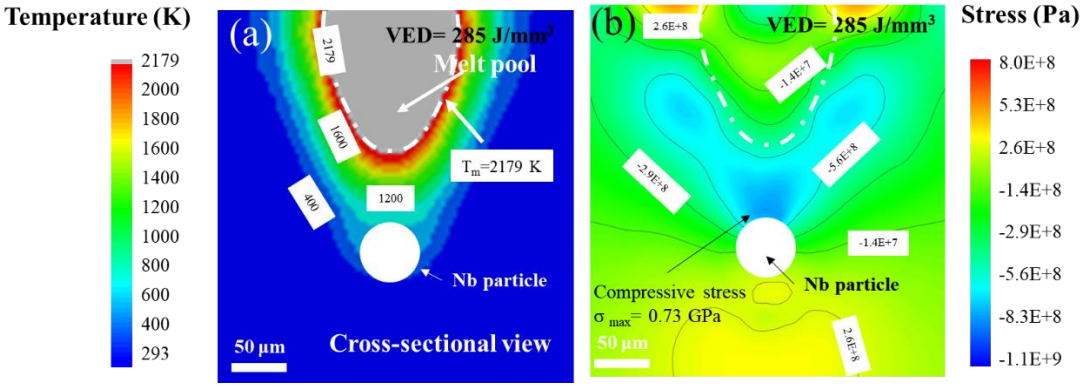

Fig. S3 Simulated temperature field (a) and thermal stress field (b) under heterogeneous model with unmelted Nb particles and VED=285 J/mm^3

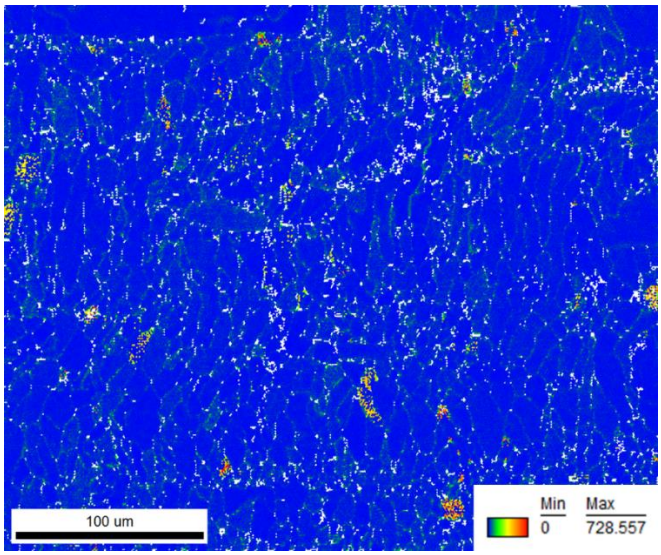

Fig. S4 GNDs density distribution of the SLM $V_{0.5}Nb_{0.5}ZrTi$ alloy. The color bar in GNDs maps indicates the range of GND density from 1 × 10^{12} m^{-2} to 728 × 10^{12} m^{-2}.

Table S1

Thermal conductivity of Zr and Nb[12].

Temperature, (K)	Thermal conductivity, K ($Wm^{-1}K^{-1}$)	
	Zr	Nb
25	23.2	53.7
400	21.6	55.2
600	20.7	58.2
800	21.6	61.3
1000	23.7	64.4
1200	26.0	67.5
1400	27.9	70.5
1600	29.7	73.6
1800	31.4	76.5

Table S2

Properties of Zr and Nb[13].

Properties	Zr	Nb
Density ρ (kg/m^3)	6520	8570
Melting point, T_m (K)	2128	2750
Specific heat capacity, c ($\times 10^3$ J $kg^{-1}K^{-1}$)	0.278	0.265
Thermal expansion coefficient, α (K^{-1})	5.7×10^{-6}	7.3×10^{-6}
Young's modulus, E (GPa)	97.1	104.9
Poisson's Ratio, v	0.38	0.397

References

[1] Gu D, He B. Finite element simulation and experimental investigation of residual stresses in selective laser melted Ti–Ni shape memory alloy[J]. Computational Materials Science, 2016, 117: 221-232.

[2] Martinson P, Daneshpour S, Koçak M, Riekehr S, Staron P. Residual stress analysis of laser spot welding of steel sheets[J]. Materials & Design, 2009, 30(9): 3351-3359.

[3] Yu G, Gu D, Dai D, Xia M, Ma C, Shi Q. On the role of processing parameters in thermal behavior, surface morphology and accuracy during laser 3D printing of aluminum alloy[J]. Journal of Physics D: Applied Physics, 2016, 49(13): 135501.

[4] Li N, Zhang J, Xing W, Ouyang D, Liu L. 3D printing of Fe-based bulk metallic glass composites with combined high strength and fracture toughness[J]. Materials & Design, 2018, 143: 285-296.

[5] Tolochko N K, Khlopkov Y V, Mozzharov S E, Ignatiev M B, Laoui T, Titov V I. Absorptance of powder materials suitable for laser sintering[J]. Rapid Prototyping Journal, 2000, 6(3): 155-161.

[6] Xing W, Ouyang D, Li N, Liu L. Estimation of Residual Stress in Selective Laser Melting of a Zr-Based Amorphous Alloy[J]. Materials, 2018, 11(8): 1480.

[7] Papazoglou E L, Karkalos N E, Karmiris-Obratański P, Markopoulos A P. On the Modeling and Simulation of SLM and SLS for Metal and Polymer Powders: A Review[J]. Archives of Computational Methods in Engineering, 2022, 29(2): 941-973.

[8] Yilbas B S, Arif A F M. Material response to thermal loading due to short pulse laser heating[J]. International Journal of Heat and Mass Transfer, 2001, 44(20): 3787-3798.

[9] Li Y, Zhou K, Tan P, Tor S B, Chua C K, Leong K F. Modeling temperature and residual stress fields in selective laser melting[J]. International Journal of Mechanical Sciences, 2018, 136: 24-35.

[10] Yang Q, Zhang P, Cheng L, Min Z, Chyu M, To A C. Finite element modeling and validation of thermomechanical behavior of Ti-6Al-4V in directed energy deposition additive manufacturing[J]. Additive Manufacturing, 2016, 12: 169-177.

[11] Hussein A, Hao L, Yan C, Everson R. Finite element simulation of the temperature and stress fields in single layers built without-support in selective laser melting[J]. Materials & Design (1980-2015), 2013, 52: 638-647.

[12] C Y Ho R W P, P E Liley. Thermal Conductivity of the Elements: A Comprehensive Review[J]. Journal of Physical and Chemical Reference Data, 1974, 3(1-147).

[13] Lide D R. CRC Handbook of Chemistry and Physics[J]. Journal of the American Chemical Society, 2007, 129(3): 724-724.